Received: 9 January 2023 | Revised: 16 February 2023 | Accepted: 1 March 2023

DOI: 10.1111/ffe.13992

ORIGINAL ARTICLE

FFEMS Fatigue & Fracture of Engineering Materials & Structures

WILEY

Strain-controlled fatigue loading of an additively manufactured AISI 316L steel: Cyclic plasticity model and strain–life curve with a comparison to the wrought material

Marco Pelegatti[1] | **Denis Benasciutti**[2] | **Francesco De Bona**[1] | **Alex Lanzutti**[1] | **Jelena Srnec Novak**[3] | **Enrico Salvati**[1]

[1]Department Polytechnic of Engineering and Architecture, University of Udine, Udine, Italy

[2]Department of Engineering, University of Ferrara, Ferrara, Italy

[3]Faculty of Engineering and Centre for Micro- and Nanosciences and Technologies, University of Rijeka, Rijeka, Croatia

Correspondence
Marco Pelegatti, Department Polytechnic of Engineering and Architecture, University of Udine, via delle Scienze 208, 33100 Udine, Italy.
Email: pelegatti.marco@spes.uniud.it

Abstract

Low cycle fatigue (LCF) regime was experimentally studied for a 316L steel additively manufactured by laser-powder bed fusion (L-PBF), a material widely used in sectors that require a reliable durability analysis. Material cyclic elastoplastic behavior is described by the Chaboche–Voce combined plasticity model, which displayed a great degree of accuracy. The fatigue life was modeled by both invoking the Manson–Coffin curve and other simplified models derived from static properties of the material; some of which showed remarkably good accuracy. A quantitative comparison with a wrought-processed 316L steel displayed a markedly different cyclic elastoplastic response but comparable fatigue strengths.

KEYWORDS

316L stainless steel, cyclic plasticity model, laser-powder bed fusion, low cycle fatigue, strain–life curves

Highlights

- Chaboche–Voce model is calibrated on experimental cyclic response of laser-powder bed fusion (L-PBF) 316L stainless steel (SS).
- L-PBF 316L SS experiences higher stress than wrought material during low cycle fatigue (LCF) loading.
- Midlife cycles of L-PBF and wrought 316L SS have similar plastic strain energy density.
- L-PBF 316L SS has a lower fatigue strength at lower strain ranges than wrought material.

1 | INTRODUCTION

Additive manufacturing (AM) of metallic materials has been sparking a growing interest in academia and many industrial sectors.[1] AM permits the achievement of unparalleled design solutions in terms of geometric complexity and shape optimization, together with rapid product development and sustainability.[2] As an example, in literature, many studies focused on optimizing AM products for different purposes under various types of loading.[3–5] Among the families of developed AM techniques, one of the most encouraging is the laser-powder bed fusion (L-PBF), distinguished by the selective melting of layers of metal powder by a laser beam to produce a final 3D object.

Nowadays, many key metallic materials have been successfully processed using L-PBF,[6] enabling a wide range of applications in several strategic industrial sectors. Some examples are the Ti6Al4V titanium alloy, largely used in the biomedical and aerospace sectors,[7–9] or the AlSi10Mg aluminum alloy, which is also considered for light-weighting and optimizing structural components in aerospace.[10–12] It is worthy of note the possibility of producing stainless steels that are among the best choices in load-bearing applications in corrosive environments—for instance, the AISI 316L stainless steel that is extensively used in critical components of nuclear reactors,[13,14] pressure vessels,[15] and aerospace.[16]

Within the families of manufacturable metallic materials by L-PBF, the structural properties of the AISI 316L steel are yet to be comprehensively understood and modeled, especially regarding its fatigue strength. Nonetheless, in the last years, many efforts have been put into fully characterizing its static properties and fatigue behavior in the high cycle fatigue (HCF) regime. In addition, accurate geometrical optimization of a structural component can be only attained if in-depth knowledge of the mechanical properties of the metallic material is available. To achieve this goal, the correct choice of the material constitutive model is of paramount importance, along with its accurate calibration, as highlighted by Li et al.[5] These assertions are particularly valid when dealing with plastic deformation in the low cycle fatigue (LCF) regime, often experienced in critical components employed in nuclear reactors, aerospace, pressure vessels, and even energy absorber. In fact, only a few, and often incomparable results, can be found in the literature for this additively manufactured material. For instance, fundamental studies of the LCF performance of L-PBF AISI 316L can be found concerning the influence of: the following thermal treatment,[17,18] specimen geometry,[19] microstructure,[20] coating,[21] layer orientation, surface roughness,[22] process parameters,[23] and high strain ranges.[24] Other further studies focused their attention on the deformation mechanisms involved during cyclic loading to reveal the role of the cell structure, which distinguishes the as-built microstructure of some AM alloys, on the LCF strength.[25] Nevertheless, the exploitation of this knowledge for structural design purposes is far from being attained. A rational selection and calibration of a cyclic elastoplastic material response model are still required to enable structural engineers to assess stress/strain states and LCF performance in real engineering applications.

The present work has a twofold objective to tackle this outstanding issue. Firstly, it targets to describe the cyclic plastic response of the AISI 316L stainless steel by means of elastoplastic models suitable for being readily implemented in finite element (FE) analysis, which are the nonlinear Chaboche and Voce models for the kinematic and isotropic hardening, respectively. Secondly, it aims to evaluate strain–life curves by simple approximate models calibrated on static properties or hardness, namely, Universal Slopes Equation (USE),[26,27] Modified USE,[28] the Roessle–Fatemi hardness method,[29] and the Medians method.[30] While the accuracy of these models is extensively discussed in the literature for metals produced by conventional manufacturing processes, to the best of the authors' knowledge no attempts have been made so far concerning AM materials; a first attempt is proposed herein. Eventually, a quantitative comparison between L-PBF steel and wrought steel is presented in terms of both cyclic elastoplastic behavior and LCF strength. This comparison is of great importance to understand how reliably AM can be used to replace the conventionally produced AISI 316L stainless steel.

2 | MATERIAL AND EXPERIMENTAL SETUP

LCF results and experimental dataset are the same as those reported in an authors' previous work,[31] which constitutes a companion study of the present article. For the sake of clarity, the main aspects related to the analyzed material are briefly summarized in the following. Cylindrical rods of AISI 316L stainless steel were vertically produced by L-PBF (Concept Laser M2 Cusing machine) using the process parameters fully given in Pelegatti et al.[31] The "island" scanning strategy was adopted to melt the powder in each layer, with a 90° rotation and 1 mm shift between successive layers. Before the removal from the building platform, a stress relief treatment at a temperature of 550°C for 6 h was performed on the rods. By drawing on standard ASTM E606/E606M-21 protocol, the cylindrical rods were turned into dog-bone specimens, with a diameter of 10 mm in the gauge section and a gauge length of 25 mm. The measured density was higher than 99.9%, based on Archimedes' method.

LCF tests were carried out in strain control at room temperature and consisted of symmetrical tension–compression loading at eight different strain amplitudes (0.3%, 0.4%, 0.5%, 0.6%, 0.7%, 0.8%, 1%, and 1.2%). For each test, the strain rate was maintained at a constant value of 0.004 s^{-1} by varying the frequency of the imposed strain waveform. The equipment for the LCF test consisted of an MTS 810 System servohydraulic machine with a 100 kN load cell and an MTS 634 model axial extensometer with 25 mm gauge length. Stress–strain cycles were acquired at selected numbers of cycles following a logarithmic pattern. Maximum and minimum stress values of all cycles were also recorded throughout each test. Indeed, stress–strain evolutions over cycles are required to investigate the elastoplastic response of the materials and to calibrate the parameters of cyclic plasticity models. Examples of stress–strain cycles recorded at strain amplitudes 0.3%, 0.6%, and 1.2% are depicted in Figure 1A. It is worth reminding from the authors' previous work[31] that, for each strain amplitude tested, the L-PBF AISI 316L steel exhibits a very brief hardening behavior followed by a continuous cyclic softening until final failure, as shown in Figure 1B. As no material stabilized state is clearly visible, the stress–strain cycles at half-life are conventionally assumed to represent the stabilized state. This assumption is a common practice because in such situation the half-life cycles represent the average cycling behavior, as reported by Manson and Halford.[27] Furthermore, this choice seems reasonable as the softening rate becomes slower and slower as the number of cycles increases and the maximum stress approach a quasi-plateau. This last statement can be verified by replacing the logarithmic scale with a linear scale in Figure 1B. Other materials exhibit a similar cyclic softening response with a quasi-stabilized state.[32,33]

Finally, for the sake of comparison with the "wrought" variant of this steel, a perfectly comparable dataset obtained in a recent study by the authors was considered, using identical sample geometry and testing conditions.[34] Figure 2A,B shows the typical microstructure of additively manufactured specimens compared with the wrought material. In the additively manufactured material, it is possible to observe a microstructure composed by an overlay of microweld beads produced by the laser scans. The microstructure inside each weld bead presents submicrometric sized columns of austenite contoured of delta ferrite as a result of micro segregation during the solidification process. The direction of column growth is related to the laser parameters, as scanning speed, heat input, and beam focus. During the analysis, some areas with cellular microstructure are evidenced and usually are related to grain columnar growth perpendicular to the analysis field. It is to highlight that the stress relief treatment does not alter the microstructure of

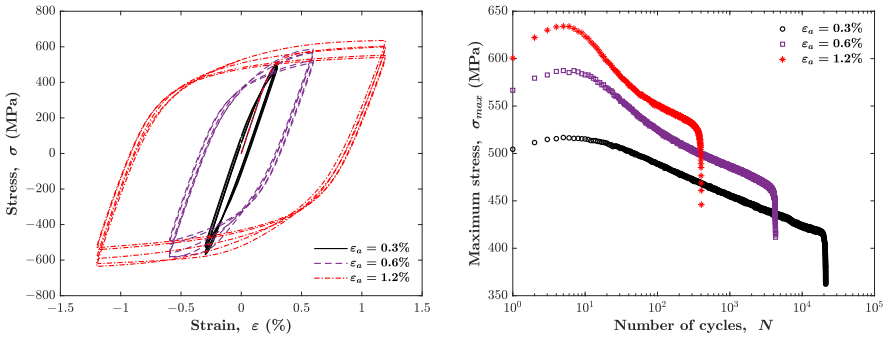

FIGURE 1 Cyclic elastoplastic behavior of laser-powder bed fusion (L-PBF) AISI 316L for three different low cycle fatigue (LCF) tests (strain amplitudes of 0.3%, 0.6%, and 1.2%): (A) 1st, 5th, 20th, 100th, and 200th stress–strain cycles and (B) maximum stress versus the number of cycles. [Colour figure can be viewed at wileyonlinelibrary.com]

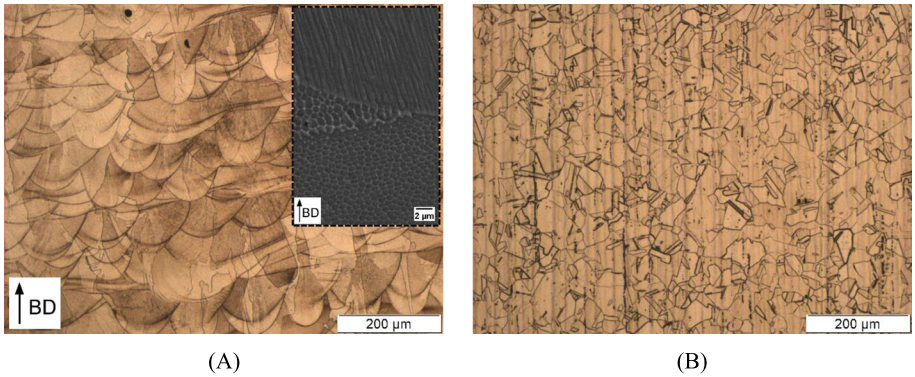

FIGURE 2 Microstructure of tested materials: (A) optical micrograph of laser-powder bed fusion (L-PBF) AISI 316L steel with a scanning electron microscopy (SEM) image as a close-up of cellular structure (BD: building direction) and (B) optical micrographs of wrought AISI 316L steel. [Colour figure can be viewed at wileyonlinelibrary.com]

the AM material. However, the microstructure is typically produced by solidification under super-cooling conditions. On the other hand, the wrought material presents equiaxic austenite grains with some stringers of delta ferrite usually located along some visible deformation bands. In the last case, the microstructure corresponds to a material that underwent a solubilization treatment after plastic deformation.

3 | CHABOCHE–VOCE CYCLIC PLASTICITY MODEL

Cyclic plasticity models can simulate the elastoplastic behavior of materials subjected to cyclic loading. In order to properly describe the behavior of various metallic materials, several cyclic plasticity models have been developed and further improved over the years.[35–37] For the sake of brevity, only the main equations of the Chaboche–Voce model are summarized in the following.

The Von Mises yield surface, which corresponds to the boundary of the elastic region, is expressed as follows[38]:

$$\sqrt{\frac{3}{2}(\boldsymbol{\sigma}' - \boldsymbol{X}) : (\boldsymbol{\sigma}' - \boldsymbol{X})} - R - \sigma_{y,0} = 0 \tag{1}$$

where $\boldsymbol{\sigma}'$ is the deviatoric stress tensor and $\sigma_{y,0}$ the initial yield stress before any loading. The second-order tensor $\boldsymbol{X}$ and the scalar value R are the variables associated to kinematic and isotropic hardening model, respectively.

The nonlinear model proposed by Chaboche[38,39] specifies the evolution of the kinematic hardening variable (back stress), $\boldsymbol{X}$:

$$\boldsymbol{X} = \sum_{i=1}^{M} \boldsymbol{X}_i; \mathrm{d}\boldsymbol{X}_i = \frac{2}{3} C_i \mathrm{d}\boldsymbol{\varepsilon}_{pl} - \gamma_i \boldsymbol{X}_i \mathrm{d}p \text{ with } M = 1, 2, 3, \ldots \tag{2}$$

The model combines M variables $\boldsymbol{X}_i$ governed by the Armstrong–Frederick model.[40] In literature, $M = 3$ is suggested as a satisfactory choice to model the nonlinear stress–strain response in cycles.[39,41] Each $\boldsymbol{X}_i$ is controlled by only two material parameters C_i and γ_i. The increment of the kinematic hardening variable, $\mathrm{d}\boldsymbol{X}_i$, during plastic loading depends on the increment of the plastic strain tensor, $\mathrm{d}\boldsymbol{\varepsilon}_{pl}$, and the accumulated plastic strain, $\mathrm{d}p$, defined as follows:

$$\mathrm{d}p = \sqrt{\frac{2}{3} \mathrm{d}\boldsymbol{\varepsilon}_{pl} : \mathrm{d}\boldsymbol{\varepsilon}_{pl}} \tag{3}$$

where $\mathrm{d}p$ is integrated during the plastic loading history.

To calibrate the model parameters, the uniaxial expression must be obtained upon integration[38,39]:

$$X = \sum_{i=1}^{M} \zeta \frac{C_i}{\gamma_i} + \left(X_{i,0} - \zeta \frac{C_i}{\gamma_i} \right) e^{-\zeta \gamma_i \left(\varepsilon_{pl} - \varepsilon_{pl,0} \right)} \tag{4}$$

where the coefficient $\zeta = \pm 1$ depends on the direction of plastic flow ($+1$ for tensile and -1 for compressive loading). Variables $X_{i,0}$ and $\varepsilon_{pl,0}$ represent the initial values of the back stress and plastic strain. Substituting Equation (4) for both tensile and compressive loading gives the following[38,39]:

$$X_a = \sum_{i=1}^{M} \frac{C_i}{\gamma_i} \tanh\left(\gamma_i \varepsilon_{pl,a} \right) \tag{5}$$

relating the uniaxial back stress amplitude X_a in stabilized condition to the plastic strain amplitude of $\varepsilon_{pl,a}$.

The isotropic hardening is described with a superposition of Z nonlinear Voce models[42]:

$$R = \sum_{i=1}^{Z} R_i; \ \mathrm{d}R_i = b_i (R_{\infty,i} - R_i) \mathrm{d}p \text{ with } Z = 1, 2, 3, \ldots \tag{6}$$

The isotropic hardening variable R is the sum of independent variables R_i, each one governed by the same type of incremental equation, though with different values of speed of stabilization, b_i, and saturated stress, $R_{\infty,i}$. Most of the times, a single variable R_i is sufficient to model the cyclic response of a material (i.e., $Z = 1$).

The incremental Equation (6) can be integrated and yields the following:

$$R = \sum_{i=1}^{Z} R_i = \sum_{i=1}^{Z} R_{\infty,i} \left(1 - e^{-b_i p} \right) \tag{7}$$

which is a sum of exponential equations. The parameter b_i controls the speed at which R_i reaches the saturated value $R_{\infty,i}$, while the accumulated plastic strain increases during plastic loading. If the material is cycled under uniaxial constant strain amplitude, the accumulated plastic strain after N cycles can be approximated as $p \cong 2\Delta\varepsilon_{pl} N$, where $\Delta\varepsilon_{pl}$ is the plastic strain range in the stabilized cycle.

4 | CALIBRATION OF MATERIAL PARAMETERS FROM EXPERIMENTAL DATA

4.1 | Elastic response and initial yield stress

At the beginning of each LCF test, the material was loaded from zero stress and strain to a predefined preset value of the strain, describing a monotonic tensile curve.

This curve was then analyzed to estimate the elastic modulus E_1 and the initial yield stress $\sigma_{y,0}$.

The elastic modulus was obtained from the linear portion of the monotonic curve through linear regression, whereas the initial yield stress was estimated by considering a plastic strain offset of 0.0025%, the same value adopted in Zhou et al.[43] The estimated values for each test were used to calculate the mean, standard deviation, and coefficient of variation (defined as the ratio between the standard deviation and the mean). The mean values of E_1 and $\sigma_{y,0}$ are equal to 198,134 and 380 MPa, respectively. The coefficient of variation for both parameters is lower than 3%.

The elastic modulus was also estimated from the stabilized stress–strain cycles. In fact, at each strain reversal, linear elastic unloading occurs with a slope equal to the elastic modulus. The estimated values from the tensile-going and compressive-going branches of a stabilized cycle are named E_{st} and E_{sc}, respectively, whereas their average is denoted as E_s. These values are required to calibrate the kinematic hardening model. The mean value, standard deviation, and coefficient of variation were also obtained for all the estimates E_{st}, E_{sc}, and E_s. The mean value of E_s is 190,513 MPa, with a coefficient of variation of 3.15%. It should be noted that the mean value of E_s estimated in the stabilized cycles is 4% lower than the mean value E_1 obtained from the monotonic curve (ANOVA test gave a p-value of 0.0122). Hales et al. indicated that this difference can be considered acceptable if it is lower than 10%.[44] Since a single value is needed to simulate the elastic response of the material, an average value of 194,323 MPa between the mean of E_1 and E_s is selected. Similarly, other authors adopted an average value among all the stress–strain cycles.[43] On the other hand, the mean value of the initial yield stress, which is equal to 380 MPa, can be directly taken in the simulation.

4.2 | Chaboche kinematic hardening model

Parameters of the kinematic hardening model were calibrated by adopting the same procedure used in Pelegatti et al.,[34] which had given satisfying results. The principal steps are outlined.

In a single stress–strain cycle, the contribution of the isotropic hardening can be considered negligible because the change in accumulated plastic strain appears to be small. Furthermore, the isotropic hardening model has already reached a saturated condition in the stabilized cycles. For these reasons, the nonlinear trend of the stress in a stress-plastic strain cycle is mainly governed by the kinematic hardening model in Equation (4).

Parameters C_i and γ_i in the equation can be estimated by fitting Equation (4) to the tensile-going or the compressive-going branch of an experimental stress-plastic strain cycle. In particular, the stabilized cycle at strain amplitude 1.2% was chosen because it provides parameters also suitable for lower strain amplitudes.[41] As already mentioned in Section 2, the cycle at $N_f/2$ was considered representative of the material stabilized condition.

From a practical point of view, the experimental compressive-going branch of the stress-plastic strain cycle was translated to the origin and mirrored to positive values. The resulting equation, which interpolates the compressive-going branch of the cycle, is as follows:

$$\begin{aligned} -\sigma+\sigma_{max}-2\sigma_{y,sc} \;&\cong X \\ =2\sum_{i=1}^{M}\frac{C_i}{\gamma_i}\frac{1-e^{-\gamma_i\varepsilon_{pl}}}{1+e^{-\gamma_i\Delta\varepsilon_{pl}}} \;&\; for\left(-\sigma+\sigma_{max}-2\sigma_{y,sc}\right)\geq 0 \end{aligned} \tag{8}$$

where σ and ε_{pl} are the stress and plastic strain values at which the fitting is applied; σ_{max} is the experimental maximum stress and $\Delta\varepsilon_{pl}$ is the plastic strain range; $\sigma_{y,sc}$ denotes the yield stress in the compressive-going branch of the half-life cycle, corresponding to a plastic strain offset of 0.01%.

After conducting the fitting procedure, the following parameters were obtained: $C_1 = 320{,}000$ MPa, $\gamma_1 = 5500$, $C_2 = 97{,}000$ MPa, $\gamma_2 = 1000$, $C_3 = 25{,}000$ MPa, and $\gamma_3 = 150$. In a stabilized cycle, the first variable X_1 describes the high initial hardening modulus at yielding, the second X_2 models the nonlinear transition at intermediate strain amplitude, and finally, X_3 controls the small slope at high strain amplitude. Their values were input in Equation (5) to check whether the fitted curve passes close to the experimental points; see Figure 3A. The experimental points $\left(\varepsilon_{pl,a}; X_a = \sigma_a - \sigma_{y,s}\right)$ are derived from the cycles at $N_f/2$ for different strain amplitudes. In the figure, $\sigma_{y,s}$ is the average yield stress between the tensile-going and compressive-going branches of the half-life cycles.

Finally, good accuracy in simulating the monotonic curve is also expected. Again, in this case, the isotropic hardening contribution is neglected, and the monotonic curve was drawn using solely the kinematic hardening model. An analytical expression for the monotonic stress–strain curve can be derived from Equation (4) with $X_{i,0} = 0$ and $\varepsilon_{pl,0} = 0$:

$$\sigma = \sigma_{y,0} + \sum_{i=1}^{M}\frac{C_i}{\gamma_i}\left(1-e^{-\gamma_i\varepsilon_{pl}}\right) \tag{9}$$

Figure 3B compares the experimental monotonic stress–strain curves for different strain amplitudes ($\varepsilon_a = 0.3\% \div 1.2\%$) to the calculated one with

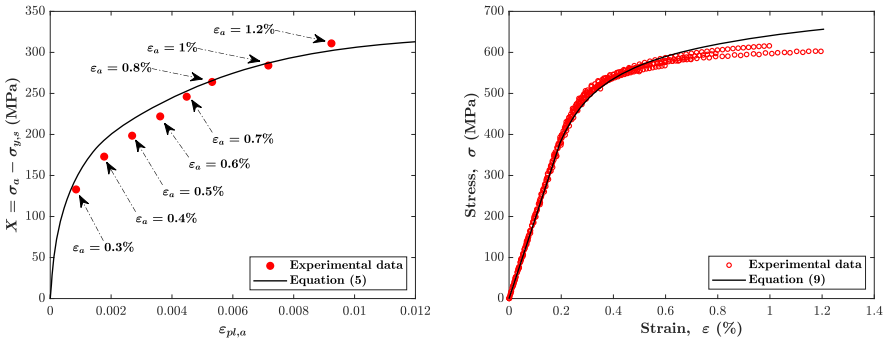

(A) (B)

FIGURE 3 (A) Contribution of the kinematic hardening model evaluated with Equation (5) compared with cyclic experimental points: $(\varepsilon_{pl,a}, \sigma_a)$. (B) Computed monotonic curve with Equation (9) compared with experimental monotonic curves for all the tested strain amplitudes: $\varepsilon_a = 0.3\% \div 1.2\%$ (open red dots). [Colour figure can be viewed at wileyonlinelibrary.com]

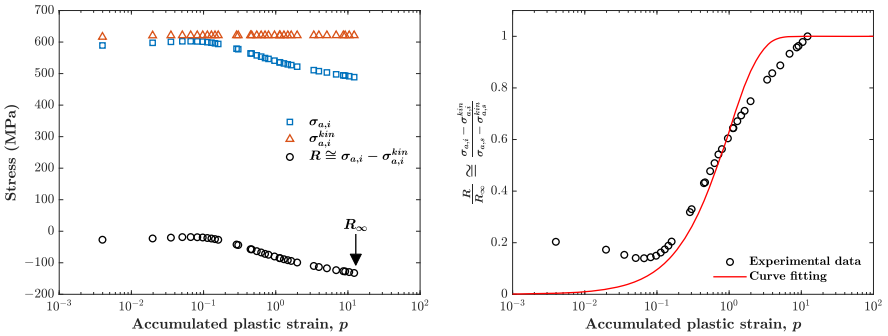

(A) (B)

FIGURE 4 Example of fitting procedure to estimate isotropic model parameters on the experimental test at the strain amplitude of 0.7%: (A) isotropic hardening contribution identified from the difference between experimental stress amplitudes and kinematic hardening contribution and (B) calibration of b with the curve fitting using Equation (11). [Colour figure can be viewed at wileyonlinelibrary.com]

Equation (9). A discrepancy between the simulated and experimental curves can be noted, mainly at higher strain values. The challenge in simulating both the stress–strain cycles and the monotonic curve using the same kinematic hardening parameters has been already reported in the literature.[45–47] Despite that, the estimated parameters in the present work can be considered sufficiently accurate for design purposes.

4.3 | Nonlinear isotropic hardening model

The evolution of the experimental stress amplitudes up to $N_f/2$ forms the basis for calibrating the isotropic hardening model. As described in a previous work,[34] the procedure to estimate the isotropic model parameters requires that the kinematic hardening contribution (computed with the parameters estimated previously) is removed from the experimental cyclic stress response. Essentially, the fitting procedure explained below is based not only on the experimental data but also on the simulation process. The uniaxial response was simulated by the algorithm described in Pelegatti et al.[34]

In the first step, the saturated stress R_∞ is determined for each strain amplitude as the difference between the experimental stress amplitudes $\sigma_{a,s}$ and the stress amplitudes $\sigma^{kin}_{a,\,s}$ calculated by considering only the kinematic model:

$$\sigma_{a,s} - \sigma^{kin}_{a,\,s} \cong R_\infty \tag{10}$$

where subscript s indicates that the quantity is evaluated at $N_f/2$.

In a second step, the speed of stabilization b is estimated through curve fitting:

$$\frac{\sigma_{a,i} - \sigma^{kin}_{a,i}}{\sigma_{a,s} - \sigma^{kin}_{a,s}} \cong \frac{R}{R_\infty} = \left(1 - e^{-bp}\right) \tag{11}$$

where $\sigma_{a,i}$ and $\sigma^{kin}_{a,i}$ are the quantities explained before referred to the i-th cycle and p is the accumulated plastic strain evaluated from experimental data. Figure 4 exemplifies the procedure for the test at 0.7% strain amplitude. In Figure 4A, the open black markers represent the difference $\sigma_{a,s} - \sigma^{kin}_{a,\,s}$ defined above. Figure 4B illustrates the curve fitting of Equation (11). In theory, the initial value of R should be zero, which does not yet occur—see the first black markers in Figure 4B. This shortcoming comes from the fact that the kinematic hardening contribution slightly overestimates the stress response in the first few cycles; see, for example, the monotonic curve in Figure 3B. If the alternative fitting procedure proposed in Lemaitre and Chaboche's book[38]—which is usually followed in literature—had been adopted, a higher stress amplitude would result in the stabilized cycle and thus the isotropic hardening parameters should be refined at a later time. On the contrary, the procedure proposed here avoids the second recalibration.

In order to further improve the accuracy of the modeling, the cyclic stress response was finally simulated using both the kinematic and isotropic hardening model with the estimated parameters. The optimal parameters R_∞ and b were then refined by minimizing the difference between the experimental and simulated cyclic stress response. Usually, it is not necessary to iterate this step more than one time.

The estimated parameters R_∞ and b are listed in Table 1. Since their values do not exhibit a large scatter across the tested strain amplitudes, it appears reasonable to describe the material behavior by the mean value for both R_∞ and b; see Table 1. To this end, R_∞ was averaged over the values of each strain amplitude, whereas b was estimated by fitting Equation (11) on all experimental data pooled together.

TABLE 1 Kinematic and isotropic hardening model parameters estimated from experimental results.

ε_a	Isotropic model		Kinematic model
	R_∞ (MPa)	b	$C_1 = 320{,}000$ MPa
0.3%	−90	0.1528	$\gamma_1 = 5500$
0.4%	−137	0.2216	$C_2 = 97{,}000$ MPa
0.5%	−148	0.3815	$\gamma_2 = 1000$
0.6%	−156	0.6393	$C_3 = 25{,}000$ MPa
0.7%	−143	0.846	$\gamma_3 = 150$
0.8%	−152	0.7362	
1%	−149	0.7731	
1.2%	−148	1.1617	
Mean value	−140	0.6128[a]	

[a]Value obtained by fitting Equation (11) to all experimental data pooled together.

4.4 | Simulated and experimental cyclic response: A comparison

An exhaustive comparison between experimental behavior and simulations is conducted by considering combined kinematic and isotropic hardening models. Simulation inputs are the elastic modulus 194,323 MPa, the initial yield stress 380 MPa, the kinematic hardening parameters in the last column of Table 1, and the average R_∞ and b for the isotropic hardening model.

The 1st and 700th simulated and experimental stress–strain cycles at $\varepsilon_a = 0.7\%$ are compared in Figure 5A, whereas Figure 5B compares the experimental and simulated cyclic stress response for several ε_a. Although the simulated maximum stresses are not very accurate in the first few cycles and the following experimental softening seems not well represented by the exponential law in Equation (7), the experimental and simulated cycle at half-life shows quite similar values of the maximum stress, as it can be appreciated in Figure 6A,B. The simulation accuracy of each investigated strain amplitude can be quantified by the mean absolute percentage error

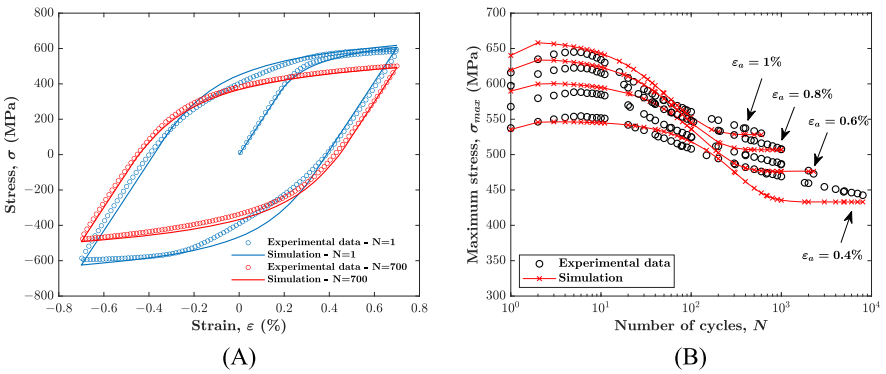

FIGURE 5 Comparison between experimental and simulated cyclic plasticity behavior: (A) 1st and 700th stress–strain cycle at $\varepsilon_a = 0.7\%$; (B) maximum stress versus number of cycles up to $N_f/2$ for four different strain amplitudes. [Colour figure can be viewed at wileyonlinelibrary.com]

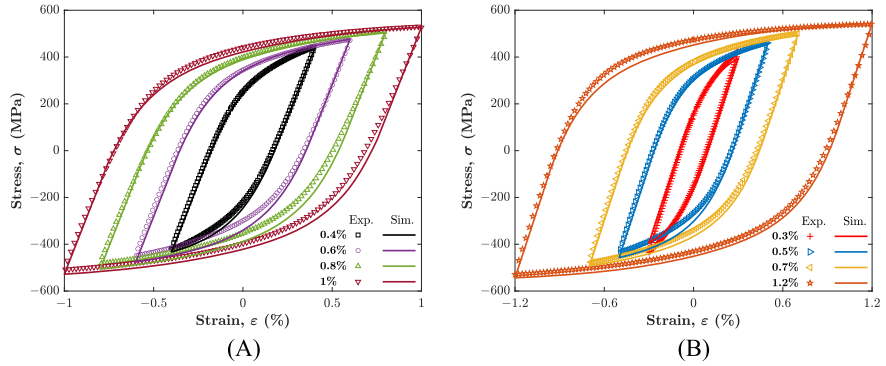

FIGURE 6 Comparison between experimental and simulated cycles at $N_f/2$: (A) 0.4%, 0.6%, 0.8% and 1%; (B) 0.3%, 0.5%, 0.7%, and 1.2%. [Colour figure can be viewed at wileyonlinelibrary.com]

(MAPE) on the maximum stresses of each considered cycle:

$$\mathrm{MAPE} = \frac{100}{l}\sum_{i=1}^{l}\left|\frac{\sigma_{max,i}^{sim} - \sigma_{max,i}^{exp}}{\sigma_{max,i}^{exp}}\right| \quad (12)$$

where l is the total number of cycles taken into consideration to calculate the index for a single strain amplitude, $\sigma_{max,i}^{exp}$ is the i-th experimental maximum stress, and $\sigma_{max,i}^{sim}$ is the i-th simulated maximum stress. Note that only few cycles are considered for a single strain amplitude and the index i is not coincident with the number of the cycle N.

In addition to MAPE index, Table 2 also lists the absolute percentage error (APE) of the first and last simulated value of maximum stress (i.e., at $N = 1$ and $N = N_f/2$) for each strain amplitude. The highest percentage error is less than 10% and is found for the first maximum stress at the strain amplitude $\varepsilon_a = 1.2\%$.

With the identified parameters of the kinematic hardening model, the shape of experimental cycles at $N_f/2$ is described precisely. Figure 6A,B confirms that the simulated stress–strain cycles (continuous lines) for each strain amplitude almost overlap with the experimental data (markers). This assures that also the simulated plastic strain energy density per cycle—a parameter used later on—corresponds with the experimental value.

5 | STRAIN–LIFE CURVE: MANSON–COFFIN MODEL AND SOME PRACTICAL APPROXIMATIONS

In the authors' previous study,[31] the experimental strain amplitude-life data were used to estimate the Manson–Coffin model[48]:

$$\varepsilon_a = \varepsilon_{el,a} + \varepsilon_{pl,a} = \frac{\sigma_f'}{E}\left(2N_f\right)^{b'} + \varepsilon_f'\left(2N_f\right)^{c'} \quad (13)$$

where $\varepsilon_{el,a}$ and $\varepsilon_{pl,a}$ are the elastic and plastic strain amplitudes. In Equation (13), the elastic part is ruled by the fatigue strength coefficient σ_f' and exponent b' and the plastic part by the fatigue ductility coefficient ε_f' and exponent c'. The estimated parameters are reported in Table 3.

When experimental fatigue data are not available to calibrate the Manson–Coffin equation (as it often happens in early design phases), the literature offers approximate methods for correlating fatigue strength to monotonic tensile properties or hardness. These methods, though approximate, are really attractive since they do not require expensive and time-consuming fatigue tests. In the sixties, Manson and Hirschberg[26,27] were the first who thought about the possibility to use these simplified methods; they proposed a method called Universal Slopes

TABLE 2 Model accuracy, expressed by mean absolute percentage error (MAPE) and absolute percentage error (APE) index, in predicting the maximum stresses.

ε_a	MAPE	APE (first cycle, $N = 1$)	APE (last cycle, $N = N_f/2$)
0.3%	5.25%	3.59%	6.65%
0.4%	2.80%	0.391%	2.17%
0.5%	2.52%	1.79%	0.759%
0.6%	2.69%	3.87%	0.719%
0.7%	2.52%	3.89%	1.59%
0.8%	1.88%	3.72%	0.204%
1%	1.81%	3.93%	0.388%
1.2%	4.11%	8.69%	0.582%
Mean value	2.95%	3.73%	1.63%

TABLE 3 Parameters of the Manson–Coffin model and some approximated models for L-PBF AISI 316L steel.

	Parameters of strain–life equation				Goodness of fit	
Strain–life equation	σ_f'/E	b'	ε_f'	c'	R^2	e_a
Manson-Coffin[48]	0.005242	−0.0845	0.66849	−0.5965	0.9167	0.7793
USE[26]	0.006321	−0.12	0.92194	−0.6	0.8601	0.5077
Modified USE[28]	0.005401	−0.09	0.424395	−0.56	0.8811	0.9148
Hardness method[29]	0.00553	−0.09	0.526058	−0.56	0.9123	0.8243
Medians method[30]	0.004986	−0.09	0.45	−0.59	0.6644	0.8775

Abbreviations: L-PBF, laser-powder bed fusion; USE, universal slopes equation.

Equation ("USE"). The method owes its name to the constant exponents (−0.12 and −0.6) assumed for the strain–life equation, regardless of material type. Although the USE method was originally correlated to fatigue data for 29 ferrous and nonferrous materials, it turned out to be approximately correct for a variety of metallic materials, including some stainless steels. The analytical expression of the USE model is directly reported here in terms of strain amplitudes and the number of reversals to failure:

$$\varepsilon_a = 1.9018\frac{UTS}{E}(2N_f)^{-0.12} + 0.7579D^{0.6}(2N_f)^{-0.6} \quad (14)$$

The strain–life equation is defined by the following static material properties: ultimate tensile strength UTS, elastic modulus E, and ductility D. Ductility is defined as $D = \ln[100/(100-\%Z)]$, in which $\%Z$ is the area reduction in the specimen cross-section. The USE model assumes that the HCF behavior of the material is driven by its static properties, while the LCF behavior is governed by ductility.

After nearly 20 years, Muralidharan and Manson[28] tested additional 50 different materials with the intention of re-examining and improving the USE model accuracy; eventually, the following expression was obtained:

$$\varepsilon_a = 0.623\left(\frac{UTS}{E}\right)^{0.832}(2N_f)^{-0.09} + 0.0196(D)^{0.155}\left(\frac{UTS}{E}\right)^{-0.53}(2N_f)^{-0.56} \quad (15)$$

named as "Modified USE". Compared with the USE model, the two exponents have slightly changed to −0.09 and −0.53, whereas the second term representing the plastic component now depends on static properties, too.

More recently, other methods were proposed for obtaining a first approximation of the strain–life curve of steels. Among them, in 2000, Roessle and Fatemi[29] suggested using the same exponents as the Modified USE, but they expressed the Manson–Coffin coefficients as a function of the sole Brinell hardness HB:

$$\varepsilon_a = \frac{4.25(HB)+225}{E}(2N_f)^{-0.09} + \frac{0.32(HB)^2 - 487(HB) + 191000}{E}(2N_f)^{-0.56} \quad (16)$$

Finally, Meggiolaro and Castro[30] devised an equation for steels in which the four coefficients of Equation (13) are approximated by the medians evaluated on a large dataset of 724 steels, which lead to the name Medians method. The only exception is the fatigue strength coefficient σ_f', which due to its high correlation with ultimate tensile strength was replaced by the median of the ratio σ_f'/UTS:

$$\varepsilon_a = 1.5\left(\frac{UTS}{E}\right)(2N_f)^{-0.09} + 0.45(2N_f)^{-0.59} \quad (17)$$

Nevertheless, the authors' literature survey has revealed that the above approximate strain–life models were mainly applied to conventional metallic materials; to the best of the authors' knowledge, nobody has neither attempted to employ them nor to develop new approximate models for estimating the fatigue strength of AM metallic materials from static tensile properties.

The results that follow then represent a first attempt applied to the L-PBF AISI 316L steel studied in this work; its strain–life curve was assessed directly from static tensile properties: $E = 198{,}562$ MPa, $UTS = 660$ MPa, and $\%Z = 75\%$, or the measured Vickers hardness $HV = 215$, which was converted into Brinell hardness $HB = 205$ by the relationship[49]: $HV = 8.716 + 0.963(HB) + 0.0002(HB)^2$.

The estimated parameters for these models are reported in Table 3, along with those of the Manson–Coffin model. The last two columns of the table report two metrics adopted to quantify the accuracy of the approximated models. The first metric is the coefficient of determination[50]:

$$R^2 = 1 - \frac{\sum_{i=1}^{n}(y_i - \hat{y}_i)^2}{\sum_{i=1}^{n}(y_i - \bar{y})^2} \quad (18)$$

where $y_i = \log(2N_{f,i})$ and $\hat{y}_i = \log\left(2\hat{N}_{f,i}\right)$ are the logarithm of the experimental and estimated number of reversals to failure, whereas $\bar{y}$ is the sample mean of y_i and n the number of experimental data. The best model has the smallest error sum of squares: $\sum_{i=1}^{n}(y_i - \hat{y}_i)^2$ and thus the highest R^2.

The second metric is the error measure proposed by Park and Song[51]:

$$e_a = \frac{(1-|\theta_1|) + (1-|1-\theta_2|) + (1-|1-\theta_1-\theta_2|) + (1-|1-r|)}{4} \quad (19)$$

where θ_1 and θ_2 define a linear regression line $\log(2N_{f,p}) = \theta_1 + \theta_2\log(2N_f)$ used to fit the relationship between the predicted and experimental number of reversals to failure, $2N_{f,p}$ and $2N_f$, respectively. Parameter r is the correlation coefficient returned by the regression analysis. Metric e_a measures the "average" difference of $2N_{f,p}$ from $2N_f$. An ideally exact strain–life model would give prediction values $2N_{f,p}$ lying on a 45° line in a plane $2N_{f,p} - 2N_f$, so that the linear regression line would have

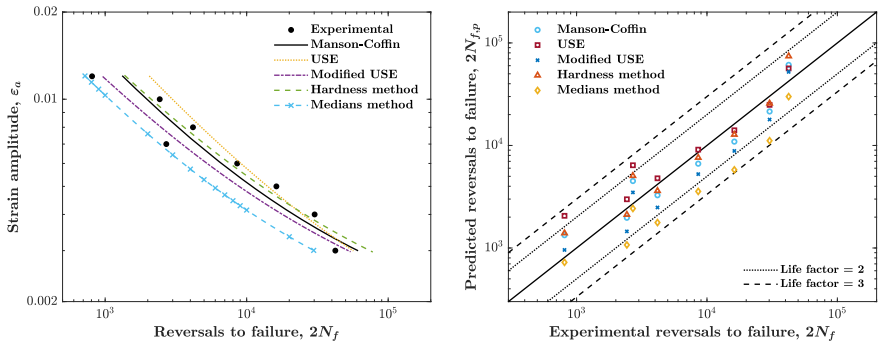

(A) (B)

FIGURE 7 Comparison between Manson–Coffin model and approximated models: (A) strain–life curves and experimental data; (B) prediction of fatigue life by different models. [Colour figure can be viewed at wileyonlinelibrary.com]

$\theta_1 = 0$, $\theta_2 = 1$, and $r = 1$, and thus, $e_a = 1$. Any prediction error in the model would make e_a decrease below unity.

The various models are also compared against experimental data in Figure 7A, while Figure 7B plots the predicted fatigue lives against the experimental ones. In the same figure, the abovementioned 45° line of perfect prediction, along with the scatter bands defined for a life factor of ×2 and ×3, is also reported.

The Manson–Coffin model has the highest R^2, which is not surprising considering that the model follows a least square fitting procedure from the real fatigue data. Besides the Manson–Coffin model, the Hardness method has the highest coefficient of determination R^2, whereas the Medians method has the lowest—it also provides the most conservative estimates; see Figure 7A. However, care must be paid when interpreting the R^2 values, since it is, by definition, unable to discriminate whether a strain–life model provides overconservative or underconservative fatigue life predictions. For example, it is interesting to note that the case of USE and Modified USE models, which in spite of having comparable R^2 values, are placed almost symmetrically around the Manson–Coffin model and thus have different levels of safety in their predicted lives—in fact, the USE model is nonconservative, the Modified USE conservative. Similar considerations also apply to e_a. By examining the value of e_a, the best method surprisingly becomes the Modified USE, whereas the USE method gives a rather low value. Nevertheless, at least of the data presented here, parameter e_a seems to be not totally adequate to properly quantify the relative accuracy of strain–life models; striking is the example of the Manson–Coffin model that, based to its e_a metric, should be classified as less accurate than other approximate methods.

This apparent contradiction may follow from the least square fitting used to estimate the Manson–Coffin model, which is only reflected in R^2 but not in e_a. It has indeed to be reminded that the Manson–Coffin model is directly estimated from experimental data, representing by definition the most accurate model taken as a reference (highest R^2), even though it is true that the least square fitting was performed on the elastic and plastic part of Equation (13) separately and not on the total strain amplitude.

For the reasons highlighted above, a visual inspection of strain–life models is also recommended to draw a conclusion on their accuracy. As can be seen, the number of reversals to failure predicted by all the methods falls inside the ×3 scatter band. By contrast, the Medians and USE method predict some fatigue lives outside the ×2 scatter band, although the former has the advantage to give conservative fatigue life predictions, while the latter does not. Overall, the most appropriate model seems the Modified USE: not only it has a high value of both R^2 and e_a but it also provides slightly conservative estimates.

6 | COMPARISON OF MECHANICAL BEHAVIOR OF L-PBF AND WROUGHT AISI 316L STEELS

6.1 | Cyclic plasticity model comparison

In this section, the cyclic elastoplastic response of L-PBF AISI 316L steel is compared with that of its wrought counterpart obtained by a conventional manufacturing process. In each subsection, a single aspect of the experimental behavior is considered: cyclic stress response, monotonic stress–strain curve, and stress–strain cycles. These aspects are first examined from a phenomenological point of view and then the implications of the experimental behavior on the modeling are discussed since the considered cyclic plasticity models are phenomenological in nature.

6.1.1 | Cyclic stress response

According to Figure 8, a marked difference is observed in the cyclic stress response of L-PBF and wrought AISI 316L steels when subjected to identical LCF loadings.

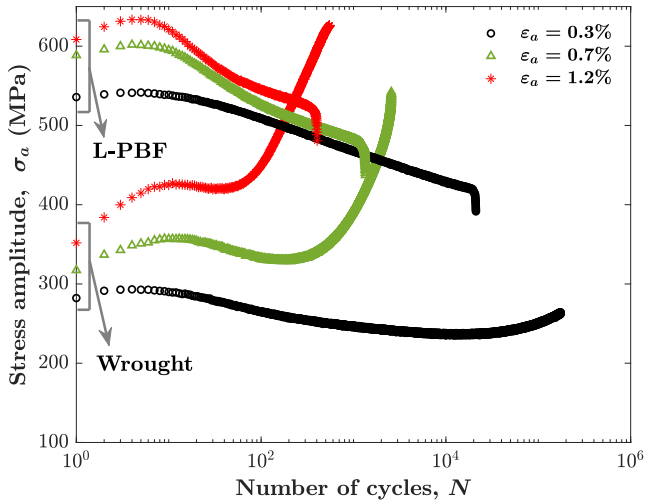

FIGURE 8 Cyclic stress response of laser-powder bed fusion (L-PBF) and wrought AISI 316L stainless steel at strain amplitude of 0.3%, 0.7%, and 1.2%. [Colour figure can be viewed at wileyonlinelibrary.com]

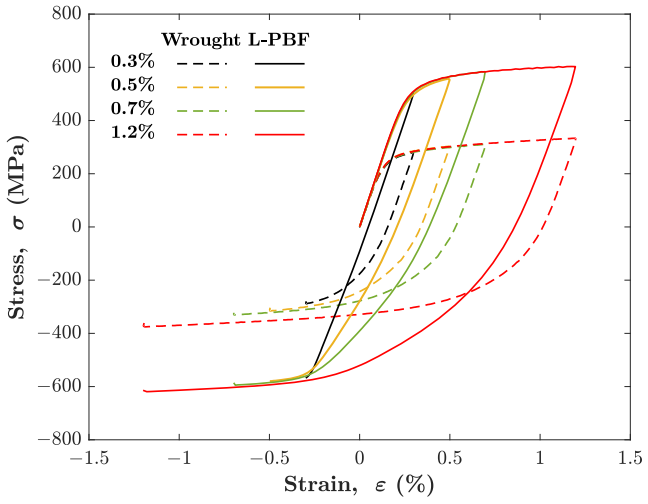

FIGURE 9 Monotonic tensile part and first load inversion at the beginning of low cycle fatigue (LCF) tests at 0.3%, 0.5%, 0.7%, and 1.2% strain amplitude, for both laser-powder bed fusion (L-PBF) and wrought AISI 316L steel. [Colour figure can be viewed at wileyonlinelibrary.com]

Figure 8 compares the cyclic response of tests at strain amplitudes 0.3%, 0.7%, and 1.2%. The L-PBF steel presents a softening behavior after a brief moderate hardening, whereas the wrought steel exhibits also a secondary hardening stage that is not as moderate as the hardening in the first cycles. The same differences in experimental behaviors are also highlighted in Yu et al.[19] As reported by the authors, from a microstructural perspective, the secondary hardening seems related to the austenite–martensite transformation caused by an intensive mechanical strain. This possible explanation was already suggested in the past.[52] However, in other works, this behavior was related to a particular dislocation arrangement, instead of a deformation induced martensite.[53] Compared with its wrought version, the L-PBF steel presents indeed a different microstructure, given its biphasic nature consisting of small columns of austenite with the presence of delta ferrite at grain boundaries. In this regard, and as also reported by other studies,[54–56] the austenite phase of L-PBF steel has a higher stability and tends to prevent secondary hardening to appear. Likely, the presence of both delta ferrite at grain boundaries and small-sized columns of austenite hinders the martensitic transformation of the austenite.

Surprisingly, the behavior of the studied AM stainless steel is similar to the wrought material subjected to cold-working,[57] although the last material presents a high amount of transformed martensite. It is evident that both materials show a higher yield strength compared with the annealed wrought material, and this initial condition seems to influence the cyclic stress response.

From a design and modeling point of view, the secondary hardening exhibited by the wrought material inevitably calls for the use of more sophisticated material models. For example, some authors[58,59] make use of a new contribution in either the isotropic or kinematic hardening part. It is also worth mentioning that the secondary hardening is usually characterized by a strain range dependence, which further complicates the modeling with the introduction of a memory surface. Additional difficulties would arise as, for instance, a less obvious interpretation and handling of simulation results in the design phase or a more elaborated calibration phase that requires one to handle a significant quantity of data to estimate the model parameters. Instead, the cyclic elastoplastic response of L-PBF AISI 316L steel is more predictable even by a standard nonlinear Voce model.

6.1.2 | Monotonic tensile curve and stress–strain cycles

The monotonic tensile curves at the beginning of the test distinctively differ for the two types of materials. Figure 9 shows that, at the same level of imposed strain, the L-PBF AISI 316L steel bears a stress level double that of wrought steel. This behavior is explained mainly by different initial yield stress, $\sigma_{y,0}$. Another characteristic is the unconventional shape of the compressive-going branch at the first loading inversion for the L-PBF material. Compared with wrought material, the elastoplastic transition in the branch is less gradual and occurs in two steps. After an initial linear unloading with slope equal to the elastic modulus, the curve keeps nearly linear but

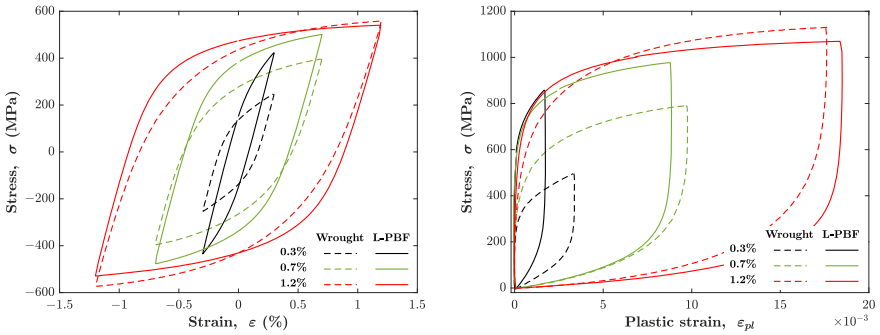

FIGURE 10 Comparison of experimental cycles at $N_f/2$: (A) stress–strain cycles and (B) stress-plastic strain cycles translated to the origin. [Colour figure can be viewed at wileyonlinelibrary.com]

with a sudden decrease in slope, until a condition resembling a complete saturation is reached; in fact, the last portion of the compressive-going branch is almost flat. This peculiar shape of the compressive-going branch is not retained in the following cycles. Apart from the difficulty in simulating this aspect with the Chaboche–Voce plasticity model, this aspect is not so relevant in the overall modeling because it only affects the first compressive-going branch and disappears in the following cycles.

Figure 10 compares the half-life stress–strain cycles at three different strain amplitudes for the wrought and L-PBF steel. For the wrought material, the cycles correspond to the secondary hardening phase of the cyclic response. Compared with its wrought counterpart, the L-PBF steel presents higher maximum and minimum stresses at strain amplitudes of 0.3% and 0.7% but similar stresses at 1.2% strain amplitude. Looking at Figure 10A is possible to understand if the wrought and L-PBF 316L steel exhibit Masing behavior. For the sake of clarity, a material displays Masing behavior if the branches of stabilized stress–strain cycles at different strain amplitudes follow the same curve.[60] Mathematically, the stabilized stress–strain cycles can be obtained homothetically from the cyclic stress–strain curve. A common practice suggests translating the stabilized stress–strain cycles at different strain amplitudes to the origin, with the lower tips being tied together. Then, if the tensile-going branches of all the stabilized cycles follow a single curve, the material has a Masing-like behavior. Figure 10B brings out the non-Masing behavior of the wrought steel, which most likely depends upon the same phenomenon that makes the secondary hardening depend upon the strain amplitude. This unusual behavior, as reported in Section 6.1.1, leads to different parameters R_∞ and b for each strain amplitude. By contrast, Figure 10B shows that the L-PBF steel follows quite nicely a Masing-like behavior.

As it is well-known, the material response in the monotonic tensile curve and stress–strain cycles can be described by the kinematic hardening model (Equation (2)). Following the suggestion of the literature,[39,41] a combination of three independent X_i was adopted for modeling the L-PBF AISI 316L steel. For the wrought steel, two X_i were used because only the strain amplitudes from 0.3% to 0.7% were considered, and thus, the third component X_3, which describes the linear slope at high strain, can be neglected without loss of accuracy. The strain amplitudes higher than 0.7% were not considered in the modeling due to the predominant secondary hardening phase. A direct comparison of kinematic hardening model parameters for L-PBF and wrought steel is thus not possible.

For that reason, a comparison of the experimental stress–strain cycles is made through another parameter, that is, the plastic strain energy density, w_{pl}. Considering a single strain amplitude for the two materials, Figure 10B shows clearly that a higher stress range gives rise to a lower plastic strain range in a cycle. Plastic strain energy density, w_{pl}, was evaluated from the experimental data, and the values are listed in Table 4. Despite the difference in stress range between L-PBF and wrought AISI 316L steel, the plastic strain energy density, w_{pl}, is similar for the cycles at $N_f/2$. This result suggests a different shape of the stress–strain cycles for the two materials. In fact, a similar plastic strain energy density in a cycle, though corresponding to different stress and plastic strain range, can be attributed to a difference in yield stress and strain hardening (the slope of the stress-plastic strain relationship loosely speaking). This observation on strain hardening is further confirmed by looking at the values taken by the loop shape parameter, V_H[61]:

$$V_H = \frac{w_{pl}}{4\sigma_a \varepsilon_{pl,a}} \tag{20}$$

An elastic perfectly plastic material has $V_H = 1$ for each cycle, whereas a material with an infinitely high strain hardening (intended here as a high ratio σ_a/σ_y) has a value approaching $V_H = 0$. Clearly, V_H depends also on the nonlinearity of the strain hardening. In fact, a

TABLE 4 Plastic strain energy density and loop shape parameter of the cycle at $N_f/2$ for each strain amplitude, calculated for L-PBF and wrought 316L steel.

	Plastic strain energy, w_{pl} (MJ/m^3)		Loop shape parameter, V_H	
Strain amplitude, ε_a	L-PBF AISI 316L	Wrought AISI 316L	L-PBF AISI 316L	Wrought AISI 316L
0.3%	1.096	1.097	0.7518	0.6578
0.4%	2.315	1.949	0.7555	0.6913
0.5%	3.680	2.887	0.7633	0.6779
0.6%	5.141	4.100	0.7729	0.6924
0.7%	6.809	5.446	0.7769	0.7085
0.8%	8.304	7.333	0.7888	0.6907
1%	12.02	10.80	0.8076	0.7322
1.2%	16.28	13.58	0.8238	0.7502

Abbreviations: LCF, low cycle fatigue; L-PBF, laser-powder bed fusion.

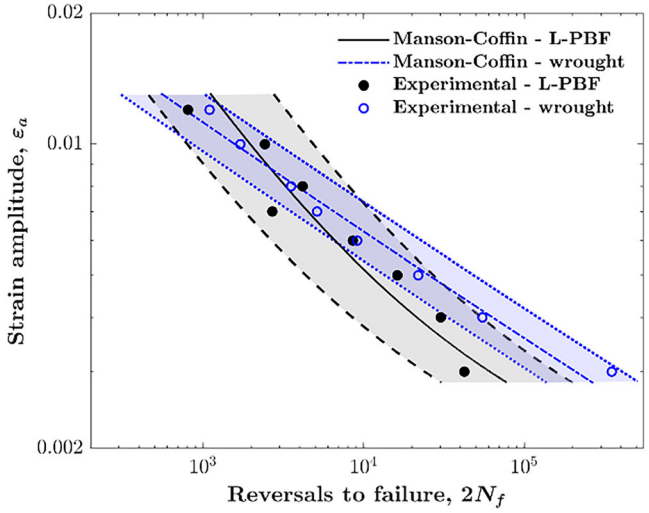

FIGURE 11 Comparison between the Manson–Coffin curves and experimental data for the L-PBF and wrought AISI 316L. The two 95% scatter bands are highlighted by transparent colors. [Colour figure can be viewed at wileyonlinelibrary.com]

material with linear strain hardening has a lower V_H value than a material with nonlinear behavior.

In Table 4, the values of V_H are reported for the cycles at $N_f/2$ for both the L-PBF and wrought 316L steel. At each strain amplitude, the AM material presents higher values (caused by a lower strain hardening) than the wrought counterpart.

6.2 | Strain–life curves

As discussed in Section 6.1, L-PBF and wrought AISI 316L steels present marked differences in their cyclic elastoplastic behavior. The question is whether such differences also reflect in the LCF strength. Figure 11 compares the Manson–Coffin curves fitted on the experimental data for L-PBF and wrought AISI 316L steel. The strain–life curves for the wrought material were estimated in a previous work.[34]

The two Manson–Coffin curves intersect each other at high strain amplitudes, then descend with two slightly different slopes. Despite that, the experimental number of cycles to failure is similar for the L-PBF and wrought AISI 316L steel, with the only noticeable deviation existing at the smallest tested strain amplitudes. In fact, the L-PBF AISI 316L steel shows a number of reversals to failure nearly 10 times lower at a strain amplitude of 0.3%.

The different scatter in fatigue lives is revealed by the different widths of the 95% scatter band of Manson-Coffin curves, see Figure 11. The scatter band is bounded by a lower and upper curve (dashed lines in Figure 11), referred to a 2.5% and 97.5% failure probability, respectively. At each strain amplitude, the scatter band is established to contain a 95% proportion of specimen failures. From a practical point of view, the scatter band was obtained by translating the elastic and plastic part of Equation (13) by 1.96 times the standard deviation estimated during linear regression. The definition corresponds to the so-called "deterministic method" and is explained in Pelegatti et al.[34] It is essential to remind that the deterministic method neglects the statistical variability of estimated regression parameters.

First, the L-PBF AISI 316L steel has a broader scatter band than the wrought material. This can be surely attributed to a larger scatter of fatigue lives coming from the larger amount of defects typical of additive manufactured products, as reported in Pelegatti et al.[31] Secondly, the two scatter bands are mostly overlapped in the tested range of strain amplitudes. At high strain amplitudes, each scatter band for one material includes almost all fatigue data of the other material, except the L-PBF test

at 0.7% strain amplitude. This conclusion is not true for the test results at 0.4% and 0.3% strain amplitude that fall outside the scatter bands of the other material. This observation suggests once more that a difference in the mechanical behavior between the two materials is more noticeable at low strain amplitudes, where the elastic contribution is predominant, and the influence of fabrication defects and other localized inhomogeneities is more pronounced, such as residual stress, material texture, and surface finish.[62,63]

7 | CONCLUSION

In this work, the cyclic plasticity behavior of a L-PBF AISI 316L steel was described by a combined nonlinear kinematic (Chaboche) and isotropic (Voce) model. The median strain–life curves were estimated by the Manson–Coffin relationship and some approximated models calibrated on static material properties. The results obtained for the L-PBF AISI 316L steel were compared with those of the same alloy in the wrought state. The following conclusions can be drawn:

- The kinematic model correctly predicts the shape of the stress–strain cycles of the L-PBF AISI 316L. Only a minor discrepancy is found in the initial tensile monotonic loading and the first compressive-going branch, where the stresses are slightly overpredicted. At the same time, the isotropic model allows the maximum stress value at half-life $N_f/2$ to be predicted correctly. However, the isotropic model relies on an exponential relationship that introduced a minor mismatch when describing the cyclic softening observed in experiments.
- The approximated strain–life models calibrated on static mechanical properties show a good matching with the LCF experimental data of the L-PBF AISI 316L. Among the considered models, the Modified USE method gives the best result in terms of predicted fatigue lives, whereas the Medians method deviates significantly from the experimental data. This attempt to extend the applicability of these simplified models to an AM material seems promising and it deserves to be investigated more extensively.
- The cyclic elastoplastic response of the wrought AISI 316L presents a secondary hardening and a dependence on the strain amplitude. On the other hand, the L-PBF AISI 316L response at $N_f/2$ could be approximated by a Masing behavior and no secondary hardening is revealed, even at higher strain amplitude.
- L-PBF and wrought AISI 316L steels exhibit comparable fatigue lives for specimens tested in the range of strain amplitudes from 0.3% to 1.2%. However, at lower strain amplitudes, the 95% scatter bands based on the Manson–Coffin curve highlight a reduced fatigue strength for the L-PBF AISI 316L compared with the wrought material.

NOMENCLATURE

AM	Additive manufacturing
APE	Absolute percentage error
b'	Fatigue strength exponent
b	Speed of stabilization
c'	Fatigue ductility exponent
C	Kinematic hardening: linear parameter
D	Ductility
e_a	Error metric for strain–life models
E	Elastic modulus
E_1	Elastic modulus at first monotonic loading
E_s	Elastic modulus at stabilized cycle
FE	Finite element
HB	Brinell hardness
HCF	High cycle fatigue
HV	Vickers hardness
LCF	Low cycle fatigue
L-PBF	Laser-powder bed fusion
MAPE	Mean absolute percentage error
N	Number of cycles
N_f	Number of cycles to failure
p	Accumulated plastic strain
R	Isotropic hardening variable
R_∞	Saturated stress of isotropic variable
R^2	Coefficient of determination
r	Correlation coefficient
USE	Universal slope equation
UTS	Ultimate tensile strength
V_H	Shape loop parameter
w_{pl}	Plastic strain energy density
$\boldsymbol{X}$	Back stress tensor
X_a	Back stress amplitude
γ	Kinematic hardening: nonlinear parameter
$\Delta\varepsilon_{pl}$	Plastic strain range
$\boldsymbol{\sigma}'$	Deviatoric stress tensor
σ	Stress
σ_a	Stress amplitude
$\sigma_{a,s}$	Stress amplitude in the stabilized cycle
$\sigma_f{}'$	Fatigue strength coefficient
σ_{max}	Maximum stress
$\sigma_{y,0}$	Initial yield stress
ε, ε_{el}, ε_{pl}	Strain (total, elastic, plastic)

ε_a, $\varepsilon_{el,a}$, $\varepsilon_{pl,a}$	Strain amplitude (total, elastic, plastic)
ε_f'	Fatigue ductility coefficient
$2N_f$	Reversals to failure
$\%Z$	Tensile test area reduction

AUTHOR CONTRIBUTIONS

Marco Pelegatti: conceptualization, formal analysis, investigation, methodology, and writing — original draft. **Denis Benasciutti**: conceptualization, supervision, and writing — review and editing. **Francesco De Bona**: conceptualization, methodology, supervision, writing — original draft, and writing — review and editing. **Alex Lanzutti**: investigation, resources, and writing — review and editing. **Jelena Srnec Novak**: methodology and writing — review and editing. **Enrico Salvati**: supervision, writing — original draft, and writing — review and editing.

ACKNOWLEDGEMENTS

Open Access Funding provided by Universita degli Studi di Udine within the CRUI-CARE Agreement.

CONFLICT OF INTEREST STATEMENT

The authors declare that they have no known competing financial interests or personal relationships that could have appeared to influence the work reported in this paper.

DATA AVAILABILITY STATEMENT

The data that support the findings of this study are available from the corresponding author upon reasonable request.

ORCID

Denis Benasciutti https://orcid.org/0000-0001-5999-5629

Enrico Salvati https://orcid.org/0000-0002-2883-0538

REFERENCES

1. Tofail SA, Koumoulos EP, Bandyopadhyay A, Bose S, O'Donoghue L, Charitidis C. Additive manufacturing: scientific and technological challenges, market uptake and opportunities. *Mater Today*. 2018;21(1):22-37.
2. DebRoy T, Wei HL, Zuback JS, et al. Additive manufacturing of metallic components—process, structure and properties. *Prog Mater Sci*. 2018;92:112-224.
3. Zhu J, Zhou H, Wang C, Zhou L, Yuan S, Zhang W. A review of topology optimization for additive manufacturing: status and challenges. *Chin J Aeronaut*. 2021;34(1):91-110.
4. Abdalla HMA, Casagrande D, De Bona F, De Monte T, Sortino M, Totis G. An optimized pressure vessel obtained by metal additive manufacturing: preliminary results. *Int J Press Vessels pip*. 2021;192:104434.
5. Li L, Zhang G, Khandelwal K. Design of energy dissipating elastoplastic structures under cyclic loads using topology optimization. *Struct Multidiscipl Optim*. 2017;56(2):391-412.
6. Ladani L, Sadeghilaridjani M. Review of powder bed fusion additive manufacturing for metals. *Metals*. 2021;11(9):1391.
7. Tomlin M, Meyer J. Topology optimization of an additive layer manufactured (ALM) aerospace part. In: *Proceeding of the 7th Altair CAE Technology Conference*; 2011, May:1-9.
8. Wang Y, Arabnejad S, Tanzer M, Pasini D. Hip implant design with three-dimensional porous architecture of optimized graded density. *J Mech des*. 2018;140(11):111406.
9. Renzo DA, Maletta C, Sgambitterra E, Furgiuele F, Berto F. Surface roughness effect on multiaxial fatigue behavior of additively manufactured Ti6Al4V alloy. *Int J Fatigue*. 2022;163:107022.
10. Orme ME, Gschweitl M, Ferrari M, Madera I, Mouriaux F. Designing for additive manufacturing: lightweighting through topology optimization enables lunar spacecraft. *J Mech des*. 2017;139(10):100905.
11. Beretta S, Patriarca L, Gargourimotlagh M, et al. A benchmark activity on the fatigue life assessment of AlSi10Mg components manufactured by L-PBF. *Mater des*. 2022;218:110713.
12. Salvati E, Tognan A, Laurenti L, Pelegatti M, De Bona F. A defect-based physics-informed machine learning framework for fatigue finite life prediction in additive manufacturing. *Mater des*. 2022;222:111089.
13. Xu L, Bao F, Zhao L, et al. Characterizing microstructural evolution and low cycle fatigue behavior of 316H austenitic steel at high-temperatures. *J Nucl Mater*. 2021;546:152758.
14. Byun TS, Garrison BE, McAlister MR, et al. Mechanical behavior of additively manufactured and wrought 316L stainless steels before and after neutron irradiation. *J Nucl Mater*. 2021;548:152849.
15. Lee HY, Kim JB, Lee JH. Thermal ratchetting deformation of a 316L stainless steel cylindrical structure under an axial moving temperature distribution. *Int J Press Vessel pip*. 2003;80(1):41-48.
16. Blakey-Milner B, Gradl P, Snedden G, et al. Metal additive manufacturing in aerospace: a review. *Mater des*. 2021;209:110008.
17. Kluczyński J, Śnieżek L, Grzelak K, et al. The influence of heat treatment on low cycle fatigue properties of selectively laser melted 316L steel. *Materials*. 2020;13(24):5737.
18. Yu C-H, Leicht A, Luzin V, Busi M, Polatidis E, Strobl M, et al. *Effect of Stress Relief Heat Treatment on Low Cycle Fatigue Behaviours of Lpbf Stainless Steel 316l*.
19. Yu C-H, Leicht A, Peng R-L, Moverare J. Low cycle fatigue of additively manufactured thin-walled stainless steel 316L. *Mater Sci Eng a*. 2021;821:141598.
20. Liang X, Hor A, Robert C, Salem M, Morel F. Correlation between microstructure and cyclic behavior of 316L stainless steel obtained by laser powder bed fusion. *Fatigue Fract Eng Mater Struct*. 2022;45(5):1505-1520.
21. Garthe K-U, Hoyer K-P, Hagen L, Tillmann W, Schaper M. Correlation between pre- and post-treatments of additively manufactured 316L parts and the resulting low cycle fatigue behavior. *Rapid Prototyp J*. 2021;28(5):833-840.
22. Shrestha R, Simsiriwong J, Shamsaei N. Fatigue behavior of additive manufactured 316L stainless steel parts: effects of layer orientation and surface roughness. *Addit Manuf*. 2019;28:23-38.

23. Kluczyński J, Śnieżek L, Grzelak K, Torzewski J, Szachogłuchowicz I, Wachowski M. The influence of process parameters on the low-cycle fatigue properties of 316L steel parts produced by powder bed fusion. *Metall Mater Trans a*. 2023;54(1):196-210.
24. Diller J, Rier L, Siebert D, Radlbeck C, Krafft F, Mensinger M. Cyclic plastic material behavior of 316L manufactured by laser powder bed fusion (PBF-LB/M). *Mater Charact*. 2022;191:112153.
25. Cui L, Deng D, Jiang F, et al. Superior low cycle fatigue property from cell structures in additively manufactured 316L stainless steel. *J Mater Sci Technol*. 2022;111:268-278.
26. Manson SS. Fatigue a complex subject: some simple approximations. *Exp Mech*. 1965;5(4):193-226.
27. Manson SS, Halford GR. *Fatigue and Durability of Structural Materials*. Materials Park: ASM International; 2006.
28. Muralidharan U, Manson SS. A modified universal slopes equation for estimation of fatigue characteristics of metals. *J Eng Mater Tech*. 1988;110(1):55-88.
29. Roessle ML, Fatemi A. Strain-controlled fatigue properties of steels and some simple approximations. *Int J Fatigue*. 2000;22(6):495-511.
30. Meggiolaro MA, Castro JTP. Statistical evaluation of strain-life fatigue crack initiation predictions. *Int J Fatigue*. 2004;26(5):463-476.
31. Pelegatti M, Benasciutti D, De Bona F, et al. On the factors influencing the elastoplastic cyclic response and low cycle fatigue failure of AISI 316L steel produced by laser-powder bed fusion. *Int J Fatigue*. 2022;165:107224.
32. Branco R, Costa JD, Antunes FV. Low-cycle fatigue behaviour of 34CrNiMo6 high strength steel. *Theor Appl Fract Mech*. 2012;58(1):28-34.
33. Marmy P, Kruml T. Low cycle fatigue of Eurofer 97. *J Nucl Mater*. 2008;377(1):52-58.
34. Pelegatti M, Lanzutti A, Salvati E, Srnec Novak J, De Bona F, Benasciutti D. Cyclic plasticity and low cycle fatigue of an AISI 316L stainless steel: experimental evaluation of material parameters for durability design. *Materials*. 2021;14(13):3588.
35. Kang G. Ratchetting: recent progresses in phenomenon observation, constitutive modeling and application. *Int J Fatigue*. 2008;30(8):1448-1472.
36. Halama R, Sedlák J, Šofer M. Phenomenological modelling of cyclic plasticity. In: Miida P, ed. *Numerical Modelling*. Rijeka: InTech; 2012:329-354.
37. Ohno N. Material models of cyclic plasticity with extended isotropic hardening: a review. *Mech Eng Rev*. 2015;2(1):14-00425.
38. Lemaitre J, Chaboche JL. *Mechanics of Solid Materials*. Cambridge: Cambridge University Press; 1990.
39. Chaboche JL. Time-independent constitutive theories for cyclic plasticity. *Int J Plast*. 1986;2(2):149-188.
40. Armstrong PJ, Frederick CO. *A Mathematical Representation of the Multiaxial Bauschinger Effect*. Vol. 731. Berkeley: Central Electricity Generating Board [and] Berkeley Nuclear Laboratories, Research & Development Department; 1966.
41. Bari S, Hassan T. Anatomy of coupled constitutive models for ratcheting simulation. *Int J Plast*. 2000;16(3-4):381-409.
42. Chaboche JL, Dang VK, Cordier G. Modelization of the strain memory effect on the cyclic hardening of 316 stainless steel. In: Jaeger A, Boley BA, eds. *Struct. Mech. React. Technol. Trans*. Vol. L; 1979:1-10.
43. Zhou J, Sun Z, Kanouté P, Retraint D. Experimental analysis and constitutive modelling of cyclic behaviour of 316L steels including hardening/softening and strain range memory effect in LCF regime. *Int J Plast*. 2018;107:54-78.
44. Hales R, Holdsworth SR, O'Donnell MP, Perrin IJ, Skelton RP. A code of practice for the determination of cyclic stress-strain data. *Mater High Temp*. 2002;19(4):165-185.
45. Krishna S, Hassan T, Naceur IB, Saï K, Cailletaud G. Macro versus micro-scale constitutive models in simulating proportional and nonproportional cyclic and ratcheting responses of stainless steel 304. *Int J Plast*. 2009;25(10):1910-1949.
46. Chaboche JL, Kanoute P, Azzouz F. Cyclic inelastic constitutive equations and their impact on the fatigue life predictions. *Int J Plast*. 2012;35:44-66.
47. Zhu Y, Kang G, Yu C. A finite cyclic elasto-plastic constitutive model to improve the description of cyclic stress-strain hysteresis loops. *Int J Plast*. 2017;95:191-215.
48. Morrow J. Cyclic plastic strain energy and fatigue of metals. In: *Internal Friction, Damping, and Cyclic Plasticity*. ASTM International; 1965.
49. Lee KS, Song JH. Estimation methods for strain-life fatigue properties from hardness. *Int J Fatigue*. 2006;28(4):386-400.
50. Ross SM. *Introduction to Probability and Statistics for Engineers and Scientists*. 6th ed. Academic Press; 2021.
51. Park JH, Song JH. Detailed evaluation of methods for estimation of fatigue properties. *Int J Fatigue*. 1995;17(5):365-373.
52. Baudry G, Pineau A. Influence of strain-induced martensitic transformation on the low-cycle fatigue behavior of a stainless steel. *Mater Sci Eng a*. 1977;28(2):229-242.
53. Man J, Obrtlík K, Petrenec M, Beran P, Smaga M, Weidner A. Stability of austenitic 316L steel against martensite formation during cyclic straining. *Procedia Eng*. 2011;10:1279-1284.
54. Hong Y, Zhou C, Zheng Y, et al. Formation of strain-induced martensite in selective laser melting austenitic stainless steel. *Mater Sci Eng a*. 2019;740:420-426.
55. Lanzutti A, Marin E, Tamura K, et al. High temperature study of the evolution of the tribolayer in additively manufactured AISI 316L steel. *Addit Manuf*. 2020;34:101258.
56. Karthik GM, Kim ES, Sathiyamoorthi P, et al. Delayed deformation-induced martensite transformation and enhanced cryogenic tensile properties in laser additive manufactured 316L austenitic stainless steel. *Addit Manuf*. 2021;47:102314.
57. Xie X, Ning D, Sun J. Strain-controlled fatigue behavior of cold-drawn type 316 austenitic stainless steel at room temperature. *Mater Charact*. 2016;120:195-202.
58. Bemfica C, Castro F. A cyclic plasticity model for secondary hardening due to strain-induced martensitic transformation. *Int J Plast*. 2021;140:102969.

59. Luo C, Zeng W, Sun J, Yuan H. Plasticity modeling for a metastable austenitic stainless steel with strain-induced martensitic transformation under cyclic loading conditions. *Mater Sci Eng a*. 2020;775:138961.
60. Yadav SS, Roy SC, Goyal S. A comprehensive review and analysis of Masing/non-Masing behavior of materials under fatigue. *Fatigue Fract Eng Mater Struct*. 2023;46(3):759-783.
61. Polák J, Obrtlík K, Hájek M, Vašek A. Cyclic stress-strain response of polycrystalline copper in a wide range of plastic strain amplitudes. *Mater Sci Eng a*. 1992;151(1):19-27.
62. Salvati E, Korsunsky AM. An analysis of macro-and micro-scale residual stresses of type I, II and III using FIB-DIC micro-ring-core milling and crystal plasticity FE modelling. *Int J Plast*. 2017;98:123-138.
63. Ye C, Zhang C, Zhao J, Dong Y. Effects of post-processing on the surface finish, porosity, residual stresses, and fatigue performance of additive manufactured metals: a review. *J Mater Eng Perform*. 2021;30(9):6407-6425.

How to cite this article: Pelegatti M, Benasciutti D, De Bona F, Lanzutti A, Novak JS, Salvati E. Strain-controlled fatigue loading of an additively manufactured AISI 316L steel: Cyclic plasticity model and strain–life curve with a comparison to the wrought material. *Fatigue Fract Eng Mater Struct*. 2023;46(6):2195-2211. doi:10.1111/ffe.13992